Water-molecule fragmentation induced by charge exchange in slow collisions with He^+ and He^{2+} ions in the keV-energy region

R. Cabrera-Trujillo
Instituto de Ciencias Físicas, Universidad Nacional Autónoma de México, Apartado Postal 48-3, Cuernavaca, Morelos, 62251, México and Quantum Theory Project, Department of Physics, University of Florida, Gainesville, Florida 32611-8435, USA

E. Deumens, Y. Öhrn, O. Quinet, and J. R. Sabin
Quantum Theory Project, Departments of Chemistry and Physics, University of Florida, Gainesville, Florida 32611-8435, USA

N. Stolterfoht
Hahn-Meitner Institut, Glienickerstraße 100, D-14109 Berlin, Germany and Quantum Theory Project, Departments of Chemistry and Physics, University of Florida, Gainesville, Florida 32611-8435, USA

(Received 4 January 2007; published 2 May 2007)

Charge exchange and fragmentation in the collision systems $He^{2+}+H_2O$ and $He^+ + H_2O$ are theoretically investigated at projectile energies of a few keV. The calculations are based on the electron nuclear dynamics (END) method which solves the time-dependent Schrödinger equation. Total and differential cross sections for charge exchange are evaluated by averaging over 10 orientations of the H_2O molecule. Summed total electron capture cross sections are found to be in good agreement with available experimental data. Projectile scattering was studied in the full angular range with respect to the incident beam direction. The theory provides a description of the fragmentation mechanisms such as Coulomb explosion and binary collision processes. For impact parameters below 3.5 a.u., we find that single and double electron capture occurs, resulting always in full fragmentation of H_2O independent of the target orientation for $^3He^{2+}$ ions. Hydrogen and oxygen fragments and its respective ions, are studied as a function of emission angle and energy. In the binary collisions regime the theoretical results are found to be in excellent agreement with previous experimental data. In the Coulomb explosion regime the theoretical data are found to peak at specific angles including 90°, which is consistent with the experiment.

DOI: 10.1103/PhysRevA.75.052702 PACS number(s): 34.50.Lf, 34.60.+z, 34.70.+e

I. INTRODUCTION

The interaction between multicharged ions and molecular targets is of great importance in several areas of research such as astrophysics, biophysics, and plasma physics. In astrophysics, collisions between bare ions in the solar wind and neutral gas molecules take place in the interstellar medium [1–4]. For α particles, which comprise one of the most abundant components of the solar wind, and with speeds in the few hundred km/s range, electron capture is the dominant process. Consequently, collisions between He^{2+} ions and molecules play an important role in most of the scenarios where solar wind interacts with cometary atmospheres. This is due to the fact that during the approach of a comet to the sun, near-surface ice starts to sublime, forming large clouds consisting mainly of water vapor.

Information about the interaction of α particles with H_2O molecules is also important for radiation damage in biological systems [5]. Since most of the energy deposited in human tissues by ion impact is absorbed by water molecules, spectra showing dissociation products of biological molecules can be interpreted by taking into account the initial interaction of the ion beam with the surrounding H_2O molecules. This leads to an increasing interest in fragmentation studies of the H_2O molecules. Fragments such as OH· radicals play a dominant role in the production of single- and double-strand breaks of DNA. To understand this process, absolute fragmentation cross sections are needed for collision systems involving water molecules.

Experimental studies of fragmentation of molecules other than H_2O have been focused on, e.g., H_2 [6–12], HD^+ [13], CO_2 [14], NO_2 [15], and CH_4 [16]. Some studies [11,12] have revealed postcollision effects by the scattered projectile, which result in an enhanced emission of fragments in the backward direction, as predicted theoretically [17,18]. Moreover, anisotropic angular distributions of the protons from fragmented H_2 have been attributed to quantum interference effects due to the identical H centers in H_2 [8] and to electron capture probabilities dependent of the molecular orientation [17].

In recent years, several experimental studies have been devoted to fragmentation of H_2O in collisions with singly [19–22] and multicharged ions [23–30]. Multiple electron capture can be identified to good approximation from the energies of the detected fragment ions. Fragments originating from the Coulomb explosion (CE) of the ionized target, as well as from quasibinary collisions, have been observed. The slow fragments, whose energy does not exceed 50 eV, originate from CE of the ionized target following electron removal at intermediate impact parameters. On the other hand, violent binary collisions involving small impact parameters produce fast fragments whose energies are well determined by two-body kinematics.

From the theoretical point of view, fragmentation of H_2 by multicharged ions has been investigated by means of clas-

sical Monte Carlo methods [17,18,31]. Molecular fragmentation studies using quantum mechanical theories face the difficulty of simultaneously treating the full coupling of the electronic and nuclear degrees of freedom. For multielectron systems, the available theoretical treatments for studying molecular fragmentation are still limited. Of those, the Car-Parinello method [32], which is based on following the dynamics on a single potential energy surface, has been applied to molecular fragmentation of water in ice [33]. The cleavage of HDO on OD and OH induced by double ionization by fast F^{7+} ions has been studied [30] in a wave-packet propagation on a numerical grid for a single potential energy surface (PES) of H_2O^{2+}. Also, studies of fragmentation of DNA produced by low-energy electrons, based on the electronic structure of the molecular system, have been carried out [34,35].

In the present work, processes of electron capture and fragmentation in slow collisions of $^3He^{2+}$ and $^3He^+$ ions with H_2O molecules are investigated. The purpose of this study is to compare quantum-mechanical calculations that involve the coupling of electronic and nuclear degrees of freedom with available experimental results. This is done in order to gain an insight into the complex mechanisms involved in the interaction of these ions with water molecules. The article is structured as follows: In Sec. II A, we provide a resumé of our theoretical approach, and in Sec. III we compare theoretical results with available experimental data in the following order: (i) electron capture probabilities, (ii) total cross sections, (iii) differential cross sections, and (iv) fragmentation. In this work all the projectile kinetic energies are given in keV, except where noted.

II. THEORETICAL APPROACH

A. Electron nuclear dynamics theory

A physically correct description of molecular reactions requires a dynamical description of both nuclei and electrons. Many meaningful approximations can be and have been defined, and some have been implemented with considerable success. The most widely used approximation consists of treating the problem of the electrons first with the nuclei fixed in a given geometry at each instant in time. This leads to the electronic structure problem in the Born-Oppenheimer approximation. This approximation, as suggested by the designation electronic "structure," describes the electronic dynamics as a succession in time of static, or more precisely, stationary structures. The forces guiding the nuclear dynamics are those of average electron dynamics. However, for systems where the coupling of the electronic and nuclear degrees of freedom might be of importance, a nonadiabatic description is required.

Considering for a moment the concepts of the most widely used theoretical description of electrons, density functional theory (DFT), we expect that in addition to tracking the changing electron density, there is an important role to be played by the momentum of the electrons. There exist extensions of DFT that try to address this to some extent, called current-density functional theory (CDFT), which recently has gained considerable attention (see [36–38], and references therein). However, CDFT focuses primarily on stationary currents associated with magnetic field effects, rather than currents associated with acceleration of electrons and electronic density. In the case of macroscopic fluids, it turns out there is a clear and clean way to derive the Navier-Stokes equations from the continuity equation and Newton's equation on a small fluid element. There is, at this time, no clear way to express the concept of acceleration of the electronic de Broglie wave in a current density equation. However, we can always rely on the Schrödinger equation to obtain many-electron wave functions.

In the 1970's, researchers tried to formulate a consistent theory of electronic states that takes into account the effect of acceleration of the electrons induced by nuclear motion. They started from the Schrödinger equation and tried to write down the correct forces and coupling terms. It took about 10 years until the authoritative review by Delos [39] settled the issue.

About 15 years ago, we introduced a systematic approach to derive the dynamical equations for moving and accelerating electrons in a straightforward and error-free way by using the time-dependent variational principle (TDVP) [40–44]. The simplest possible physical model that is relevant and applicable to molecular processes is the following model, called minimal electron nuclear dynamics (END) [45].

For molecular processes, it is an often an accurate approximation to treat the nuclei with Newtonian mechanics, using the nuclear repulsion and the Coulomb attraction with the electronic wave function to compute the forces. The electrons must obviously be treated quantum mechanically. However, for the processes considered in this paper, He-ions on water at keV energies, the electrons cannot be described by electronic stationary states, or densities. It is necessary to describe the electronic momentum as a dynamic degree of freedom. From the basic principles of quantum mechanics, for example the de Broglie wave picture, it follows that one must use complex wave functions. The simplest complex wave function is the single determinant of complex orbitals [46]. Let $\mathbf{R}_k$ and $\mathbf{P}_k$ be the positions and momenta of the nucleus k. The N-electron wave function is the determinant $\det\{\chi_i(\mathbf{x}_j,\mathbf{R}_k,\mathbf{P}_k)\}$ with complex dynamical spin orbitals $\chi_j, j=1,\ldots,K$ that are linear combinations of atomic spin orbitals $u_j, j=1,\ldots,K$. The complex expansion coefficients of the spin orbitals χ_j in terms of the basis spin orbitals u_j are then the dynamical variables of the theory, i.e., $\chi_h=u_h+\Sigma_p u_p z_{ph}$. The real parts of these complex coefficients correspond to generalized position coordinates and the imaginary parts to generalized canonical momenta. These atomic orbitals include electron translation factors to insure Galilean invariance and a proper account of charge transfer [45]. Application of the time-dependent variational principle to the action produced by the quantum mechanical Lagrangian $L=\langle\psi|i\hbar\partial/\partial t-H|\psi\rangle/\langle\psi|\psi\rangle$, with H the system Hamiltonian combined with the Euler-Lagrange equations produces the equation of motion of the dynamic variables of the system. These equations are described in detail in the review paper [45] and are solved by numerical integration in time by the program ENDYNE [47].

The END equations are a coupled set of ordinary differential equations (ODE) for the complex expansion coeffi-

cients z_{ph} and the nuclear positions $\mathbf{R}_k$ and momenta $\mathbf{P}_k$. These ODE are nonlinear and complex. Numerical algorithms exist to compute the trajectory $\{\mathbf{R}_k(t),\mathbf{P}_k(t),z_{ph}(t)\}$ in the phase space of the generalized coordinates $\{\mathbf{R}_k,\mathbf{P}_k,z_{ph}\}$ starting from an initial point $\{\mathbf{R}_k^0,\mathbf{P}_k^0,z_{ph}^0\}$. The initial state $\{\mathbf{R}_k^0,\mathbf{P}_k^0,z_{ph}^0\}$ is the electronic stationary state at the nuclear geometry $\mathbf{R}_k^0$, i.e., the coefficients z_{ph}^0 are the Hartree-Fock single determinantal wave function determined by a self-consistent field (SCF) calculation.

To analyze the electronic state of the molecular system after the reaction, we perform a projection of the single determinantal wave function on various subspaces of electronic wave functions with given electronic characteristics. After the collision, the system can be divided into fragments or clusters that no longer interact. We use the lack of interaction between fragments to decide when to stop the propagation. The properties we can specify are electronic charge, or, equivalently, number of electrons, in each fragment, and the total electronic spin of each fragment. In this paper, we specify the total charge. The norm of the projected wave function then gives the probability of finding the specified combination of charges on the fragments in the final wave function. That is, one obtains the probability P_{if} for that charge state where i and f are the initial and final charge states, respectively. Because the fragments are no longer interacting, this probability is constant in time, as no more charge flows between the fragments, even though there still may be time evolution inside some fragments, e.g., due to nuclear vibrations and rotations of the fragment. In order to compute the projected wave function, we transform to a basis of energy optimized orbitals for the fragments and compute the overlap of the evolving END state with all configurations that can be built in that basis and that are compatible with the specified charge distribution. Due to the choice of basis, the expansion converges quickly, although the projection is computationally expensive.

B. Calculation details

The target water molecule is initially placed with the oxygen atom at the origin of a Cartesian laboratory coordinate system with orientation specified by the Euler angles α, β, and γ as shown in Fig. 1.

The initial projectile velocity is set parallel to the z axis, in the xz plane, and directed towards the target with an impact parameter, b. The ion projectile starts 20 a.u. from the target, and the trajectory is evolved until the projectile is 120 a.u. past the target, which is the approximated time for the fragmentation to occur for a projectile energy of 5 keV. For lower energies, the propagation time was extended as required by the dynamics. For α particles or projectiles in an electronic S state, as in our $^3He^+$ case, the projectile orientations are not required. Thus, we need to consider only the target orientations. The $^3He^+$ ion projectile has two spin states, both of which need to be considered.

In order to obtain orientationally averaged properties, we must perform a target rotation over the Euler angles with respect to the incoming beam. A coarse set of points is obtained for increments of 90° in all the three Euler angles for a minimum of ten independent target orientations for a molecule of C_{2v} symmetry. The ten basic target orientations place the molecular bond along the xy, yz, and xz plane. In Table I, we label these ten orientations.

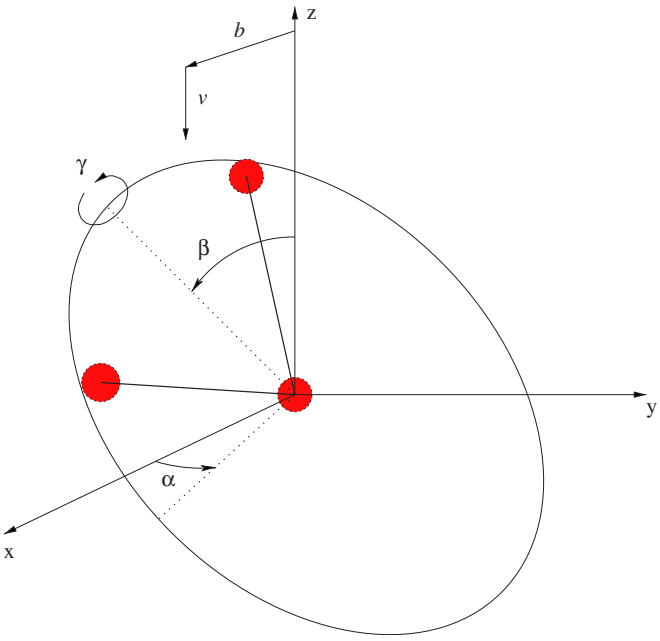

FIG. 1. (Color online) Schematic representation of the space fixed molecular coordinate frame that represents the projectile and target orientations.

The orientational average of a property g that depends on the Euler angles is given by

$$\bar{g} = \frac{1}{8\pi^2}\int g(\alpha,\beta,\gamma)\sin\beta d\alpha d\beta d\gamma. \quad (1)$$

We carry out this integral by means of the trapezoidal rule [48]. The result, for the case of a molecule with C_{2v} symmetry and with steps of $\pi/2$ for all the Euler angles, is

TABLE I. Water-molecule orientation in the space fixed axis system. (See Fig. 1.)

I1	(α=0,	β=0,	γ=0)
I2	(α=0,	β=0,	$\gamma=\pi/2$)
IIa1	(α=0,	$\beta=\pi/2$,	γ=0)
IIa2	($\alpha=\pi/2$,	$\beta=\pi/2$,	γ=0)
IIa3	($\alpha=3\pi/2$,	$\beta=\pi/2$,	γ=0)
IIb1	(α=0,	$\beta=\pi/2$,	$\gamma=\pi/2$)
IIb2	($\alpha=\pi/2$,	$\beta=\pi/2$,	$\gamma=\pi/2$)
IIb3	($\alpha=3\pi/2$,	$\beta=\pi/2$,	$\gamma=\pi/2$)
III1	(α=0,	$\beta=\pi$,	γ=0)
III2	(α=0,	$\beta=\pi$,	$\gamma=\pi/2$)

$$\bar{g} = \frac{1}{4\pi}\{(\pi - 2)(g_{I1} + g_{I1} + g_{III1} + g_{III2}) + g_{IIa1} + 2g_{IIa2} + g_{IIa3} + g_{IIb1} + 2g_{IIb2} + g_{IIb3}\}. \quad (2)$$

At the start of the calculation, the molecular target is initially in its electronic ground state ($\bar{X}^1A_1$) and equilibrium geometry, as computed in the given basis at the SCF level. The basis functions used for the atomic orbital expansion are derived from those optimized by Dunning [49,50] from the series aug-cc-pVDZ. For the hydrogen atoms, the basis set consists of $[5s2p/3s2p]$ with the addition of a diffuse s and p orbital for a better description of the long-range interaction. The exponents of these orbitals follow an even-tempered sequence to avoid linear dependencies. For the oxygen atom, we use a $[10s5p/3s2p]$ basis, and for the description of the electron capture by $^3He^{2+}$ and $^3He^+$ we use a basis set consisting of $[5s2p/3s2p]$. After a study with different basis set, these basis provided a balance between a correct description of the electronic structure and the time required for the calculation. Furthermore, we have verified that no change larger than 5% ocurred in the charge transfer or ion energy when increasing the size of the basis set, thus insuring convergence of our calculations.

For $^3He^{2+}$ projectiles, a range of impact parameter values, b, from 0.0 to 15.0 a.u. is used, which we separate in three regions. For close collisions, from 0.0 to 4.0 a.u., we use steps of 0.1 a.u. For the intermediate region, from 4.0 to 6.0 a.u., we use steps of 0.2 a.u., and for $b>6.0$, we use steps of 1.0. This gives us 60 fully dynamic trajectories for each target orientation and projectile energy. For the $^3He^+$ projectiles, the impact parameter grid from 0.0 to 3.0 a.u. has steps of 0.1, from 3.0 to 5.0 a.u. the step is 0.2 a.u., and from 5.0 to 8.0 a.u. the step is 0.5. In addition trajectories for $b=10.0$, 12.0, and 15.0 are run. For the case of orientations where the scattering angle varies quickly as a function of the impact parameter, e.g., head-on collisions, the grid was increased to take this behavior into account by making Δb smaller in the region of interest.

III. RESULTS

A. Electron capture probability for $^3He^{2+}$

After evolution of the system wave function, we calculate the mean number of electrons, $n(b,E_p)$, on the projectile as a function of the impact parameter, b, and the projectile energy, E_p, by means of the Mulliken population analysis [51]. In this analysis the electron density of a multinuclear system is partitioned for negligible overlap between atomic orbitals on different product fragments as discussed in Ref. [52].

As mentioned above, END allows for the determination of the probability of a specific reaction mechanism by projecting the system wave function onto the corresponding final state wave function. Thus, we determined the probabilities for zero, P_{22}, single, P_{21}, and double, P_{20}, electron capture by the projectile. From this, the mean number of electrons can be recovered as $n(b,E_p)=P_{21}+2P_{20}$. In Fig. 2, we show the impact parameter weighted probabilities for $^3He^{2+}$ colliding with water molecules at 5 keV for the orientation I1. The probability P_{22} is not shown since $P_{20}+P_{21}+P_{22}=1$.

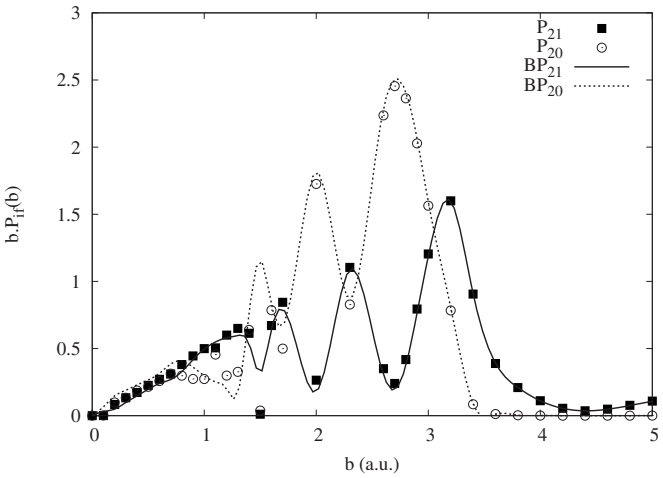

FIG. 2. Comparison of single (P_{21}) and double (P_{20}) electron capture probabilities, P_{if}, weighted by the impact parameter b as obtained by projections on the electronic wave function and the binomial distribution approximation [BP_{21} and BP_{20} from Eq. (3)] for the orientation I1 and $^3He^{2+}$ projectile energy of 5 keV.

It should be noted that channels involving ionization mechanisms are not properly described by the END approach, as the method does not yet describe free electron propagation properly. We expect that ionization of a single electron is a negligible process at the low impact energies considered here. However, ionization processes affecting two-electrons, such as transfer ionization and double capture into autoionizing states, may play a certain role. Transfer ionization involves the capture into the helium $1s$ orbital, which liberates potential energy which is used to simultaneously ionize another target electron during the collision. Double capture into autoionizing states involves the transfer of two electrons into higher-lying projectile states followed by autoionization after the collision. These channels modify the single electron capture in the projectile and thus affecting the zero and double electron capture channels. Experimental studies [26,27] have shown that transfer ionization is a significant reaction channel, whereas double capture into autoionizing states is less important for the present collision systems.

By assuming that the electron capture is governed by statistical laws resulting in a binomial distribution [53], the probabilities for zero, single, and double electron capture can be obtained as functions of the total mean number of electrons and are given by

$$P_{22} = \left(1 - \frac{n(b,E_p)}{2}\right)^2,$$

$$P_{21} = n(b,E_p)\left(1 - \frac{n(b,E_p)}{2}\right),$$

$$P_{20} = n(b,E_p)^2/4. \quad (3)$$

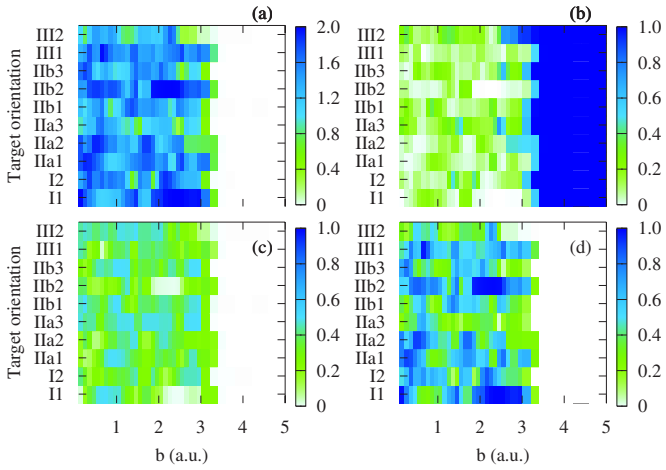

FIG. 3. (Color online) (a) Mean number of electrons, (b) zero, (c) single, and (d) double electron capture probabilities for 0.5 keV $^3He^{2+}$ ions colliding with H_2O as a function of the impact parameter b and target orientation. (See text for discussion)

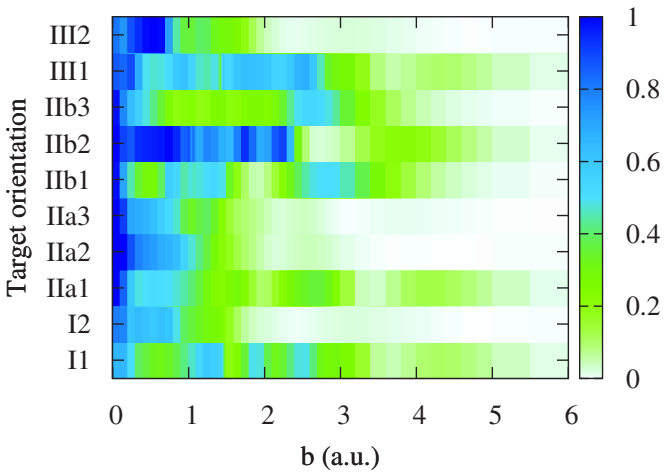

FIG. 4. (Color online) Probability for single electron capture, P_{10}, by 1 keV $^3He^+$ colliding with H_2O as a function of the impact parameter b and target orientation.

In Fig. 2, we compare the END results with the corresponding probabilities obtained using the binomial distribution assumption. We note that the two ways of determining the probabilities are in good agreement. The largest discrepancy occurs at small impact parameter where nonadiabatic effects start to be important and the binomial approximation breaks down. The contribution of this region to the cross section is small. Because the projection method to obtain the probability P_{if} is quite computationally intensive and seems not to give results significantly different from the simple assumption of a binomial distribution, we continue our analysis of electron capture probabilities based on the binomial assumption as a function of the END mean number of electrons.

In Fig. 3, we show a density plot of the mean number of electrons, $n(b,E_p)$; the zero, P_{22}; the single, P_{21}; and double, P_{20} electron capture probabilities in Figs. 3(a)–3(d), respectively. The capture probabilities are obtained using the binomial distribution assumption [Eqs. (3)] at 0.5 keV. The ordering and labeling follows that in Table I.

The most striking feature in Figs. 3(a), 3(c), and 3(d) is that electron capture occurs only for $b \leqslant 3.5$ a.u. for all the orientations and all the energies analyzed in this study. Accordingly, for $b \leqslant 3.5$ a.u. the zero electron capture probability is negligible, as seen in Fig. 3(b). For single electron capture, given in Fig. 3(c), we find in the $b \leqslant 3.5$ a.u. region a nearly uniform capture probability for all target orientations. From Fig. 3(d), we note a preferential capture of two electrons for the target orientations I1, and IIb2 around $b \sim 2.2$ a.u., which correspond to binary collisions with an H atom of the water molecule. That is, collisions where the projectile collides head on with an atomic center of the molecule, with large momentum transfer. This process is attributed to a binary collision as will be discussed in a later section. Similarly, there is significant double electron capture for most of the orientations for $b < 0.8$ a.u. that arises from the head-on collisions with an oxygen atom.

A result obtained from our study, but not shown in this work, is that for 5.0 keV projectiles we find that double electron capture is lower than in the 0.5 keV case. Furthermore, not much difference is observed for the one-electron capture, except that there is an appreciable probability of single electron capture for $b > 3.5$ a.u. by the 5.0 keV projectiles. This is a consequence of the higher projectile energy and plays an important role in the total electron capture cross section which we discuss in a later section.

B. Electron capture probability of $^3He^+$

In Fig. 4, we present the single electron capture probability, P_{10}, for the case of $^3He^+$ colliding with water for all the target orientations as a function of the impact parameter at 1 keV projectile energy. We see that the largest capture cross section occurs for orientation IIb2 where a head-on collision with a hydrogen atom occurs at $b \sim 1.5$ a.u. Meanwhile, at 5 keV, the orientations I1, IIb2, and III1 have the largest electron capture probability as a result of the head-on collision.

For all the energies analyzed, we find that the region for which the electron capture occurs is different for each target orientation, contrary to the $^3He^{2+}$ case. Depending on the target orientation, P_{10} extends over the range $0 < b < 1.0$ a.u. or $0 < b < 3.0$ a.u., contrary to the $^3He^{2+}$ case which is nearly uniform over the range $0 < b < 3.5$ a.u.

C. Total cross section for charge exchange

For a given projectile energy, the total cross section for charge exchange is obtained from the appropriate probabilities as

$$\sigma_{if}(E_p) = 2\pi \int P_{if}(b,E_p) b db, \tag{4}$$

for each target orientation. The orientational average is constructed according to Eq. (2).

In Fig. 5, we compare our orientationally averaged total cross section for electron capture (for one and two electrons), as a function of the projectile energy, with the recommended

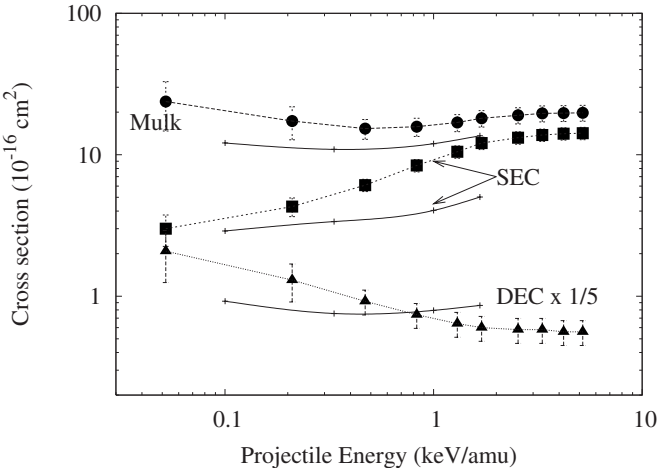

FIG. 5. Cross section for single (SEC) and double (DEC) electron capture by $^3He^{2+}$ colliding with H_2O (solid lines). Note the scaling factor 1/5 for DEC. Also shown is the Mulliken cross section $\sigma_{Mulk}=\sigma_{21}+2\sigma_{20}$ (solid circles). The experimental data (solid box) are for the SEC and (solid triangles) for the DEC from Greenwood *et al.* [54].

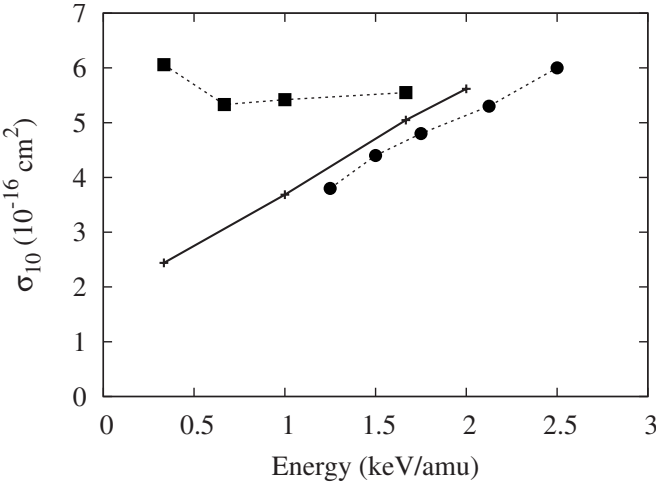

FIG. 6. Charge transfer cross sections, σ_{10}, for He^+ collisions with H_2O. Solid line, our results. Experimental data: (solid circle) Rudd *et al.* [55] and (solid square) Greenwood *et al.* [56]

experimental values of Greenwood [54]. It is seen that the experimental results are systematically higher, by some 20–30 %, than the theoretical Mulliken cross sections $\sigma_{Mulk}=\sigma_{21}+2\sigma_{20}$, whereas larger discrepancies (up to a factor of ~2) are found for the individual cross sections. These deviations are greater than the experimental uncertainties.

It is likely that the deviations between theory and experiment is explained by effects of the transfer ionization and autoionization channels missing in the END approach. For instance, autoionization after double capture enhances the single electron capture (SEC) cross sections on the cost of the double electron capture (DEC) so that the corresponding cross sections are reduced accordingly. This may explain the theoretical underestimation of the SEC and overestimation of the DEC data, respectively, at energies above ~0.5 keV. This redistribution effect is expected to cancel in the Mulliken cross section, for which the agreement between experiment and theory is indeed found to be quite good.

The calculated total cross section for single electron capture in $^3He^+ + H_2O$ collisions (i.e., neutralization, σ_{10}) is shown in Fig. 6 and is compared to the experimental determinations of Rudd *et al.* [55] and to those of Greenwood *et al.* [56]. The linear behavior shown by our results follows the experimental trend of the data by Rudd *et al.* in the high-energy range. However, our results indicate a different trend when compared with the results of Greenwood *et al.*, showing a difference up to a factor of three in the low-energy range.

Also, considering our results for single electron capture for $^3He^{2+}$, as shown in Fig. 5, we note that the results for single electron capture for $^3He^+$ and those of $^3He^{2+}$ are very similar. This conclusion is similar to that reached by Greenwood [56] from experimental evidence.

D. Projectile differential cross section

From the deflection function, $\Theta(b)$, i.e., the scattering angle as a function of the impact parameter, we calculate the differential cross sections for various scattering angles ranging from values as small as 0.01° to values as large as 100°. The lower limit of the angular range corresponds to large impact parameters and thus soft collisions involving weak perturbations. In contrast, large scattering angles correspond to small impact parameters involving close collisions of the projectile with a single target atom.

In soft collisions, quantum interferences become important due to collisions with different impact parameters leading to the same scattering angle, as well as to rainbow and glory scattering from the same orientation. Due to this and to the classical description of the nuclei, semiclassical corrections are used to take into account quantum interference effects. We have implemented the Schiff approximation [57,58] for small scattering angles, to account for the quantum effects of forward scattering (long-range interactions, large impact parameters) per orientation. We note that interference effects from different orientations are not taken into account. This is work in progress.

To implement the Schiff approximation, we require the deflection function for each orientation of the molecular target. We use the calculated deflection function obtained from the projectile trajectories together with the Schiff approximation to obtain the differential cross section per target orientation and then average over the target orientations. The use of the Schiff approximation over some other semiclassical approximations, as the Airy, uniform, or eikonal approximations [59] is due to the fact that the Schiff approximation considers the contribution of all the terms of the Born series and we have extended it to include fully dynamical trajectories instead of straight line trajectories as done in the eikonal approximation [58,60].

In Fig. 7(a), we show the orientationally averaged differential scattering cross section for single electron capture, $d\sigma_{21}/d\Omega$, for $^3He^{2+}$ colliding with water molecules at 0.5, 1, and 5 keV as a function of the laboratory angle. For scattering up to 1°, we use the Schiff approximation, and for larger angles, we use the classical differential cross section. The results show a variation of several orders of magnitude. In

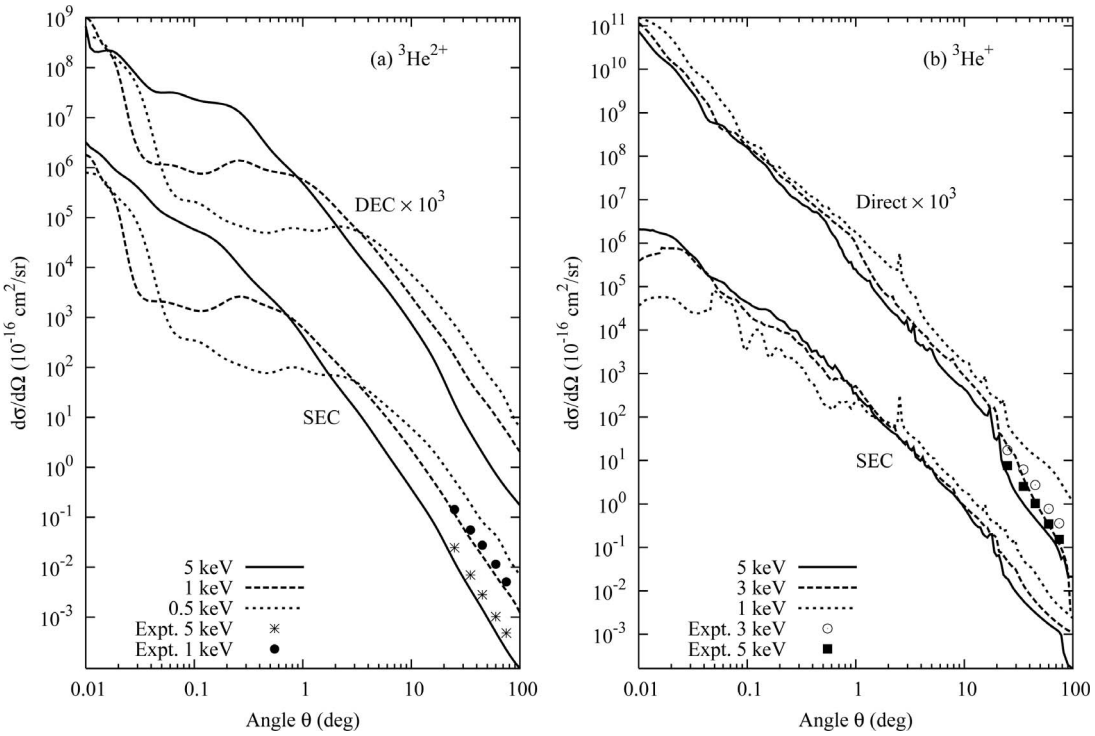

FIG. 7. (a) Orientational averaged differential cross sections for single (SEC) and double (DEC) electron capture for 0.5, 1, and 5 keV $^3He^{2+}$ scattered from H_2O molecules as a function of the laboratory scattering angle. In (b) we show the orientational averaged direct and one electron capture differential cross section, for $^3He^+$ ions at 1, 3, and 5 keV colliding with H_2O. The experimental data are from Ref. [26] for $^3He^{2+}$ at 1 and 5 keV, and the data for $^3He^+$ are from Ref. [25] at 3 and 5 keV.

the region of small scattering angles the data show structure, which is the results of quantum interference effects.

For scattering angles between 0.05° and 1°, we note that $d\sigma_{21}/d\Omega$ presents a valley that becomes more pronounced for lower projectile energies. The larger contribution to the single electron capture occurs for $b<3.5$ a.u., which corresponds to scattering angles larger than 1°. Also, we compare with available experimental data from Ref. [26] for scattering angles from $\theta\sim 20°$ to 90° for 1 and 5 keV. For 5 keV, the theoretical results are within 30% of the experimental data and for 1 keV within 10%. Again, we may attribute these discrepancies to the ionization channels missing in the END approach.

In Fig. 7(a) we also show the results for the double electron capture differential cross section, $d\sigma_{20}/d\Omega$, for the same range of energies. From these results we also note a more pronounced valley for scattering angle between 0.03° and 1°. Also, in both cases ($d\sigma_{21}/d\Omega$ and $d\sigma_{20}/d\Omega$), there is an inversion of the curves around $\theta\sim 1°$ for different projectile energies. That is, comparing the 5 keV differential cross section at small angles it is higher than the 1 keV case, while for the large scattering region the inverse is true. From these results we see that single and double electron capture are predominant at large scattering angles or intermediate to small impact parameters, in agreement with Fig. 3.

The END results for the direct differential cross section, $d\sigma_{11}/d\Omega$, for $^3He^+$ projectiles are displayed in Fig. 7(b) and are compared with experimental results [25]. The agreement between theory and experiment is satisfactory. Again, the Schiff approximation is employed for scattering angles below 1°, while the classical cross sections are displayed for larger angles. In the same figure, we display the theoretical results for the one electron capture differential cross section, $d\sigma_{10}/d\Omega$. In this case there are no experimental results available for comparison. The inversion effect of the curves for several projectile energies, as seen in the case of $^3He^{2+}$, is also observed around $\theta\sim 1°$. Also, the peaks produced by the rainbow scattering in the classical differential cross section, are more pronounced for $\theta>1°$ than in the $^3He^{2+}$ case which are softened by the two electron capture. All foregoing discussion has been concerned with projectile processes, we now turn to a discussion of what happens to the molecular target.

E. Mechanisms for fragmentation

From the final wave function and final momentum, $\mathbf{P}_k$, for each nucleus, we calculate the number of particles ejected as a function of angle and corresponding ion energy. These results are presented in Figs. 8–10.

Figures 8–10 contain a large amount of computed data in very compact form. In order to help in understanding the graphic display in the two right-hand panels of Fig. 8 (similar considerations apply to Figs. 9 and 10), one might consider a fixed fragment energy, say 100 eV. What the graphics show is that oxygen fragments with that kinetic energy are scattered exclusively at angles between 60° and 70°, while the hydrogen fragments are scattered predominantly in a narrow range around 70°, but with some being ejected in some narrow ranges at smaller and larger angles. This type of

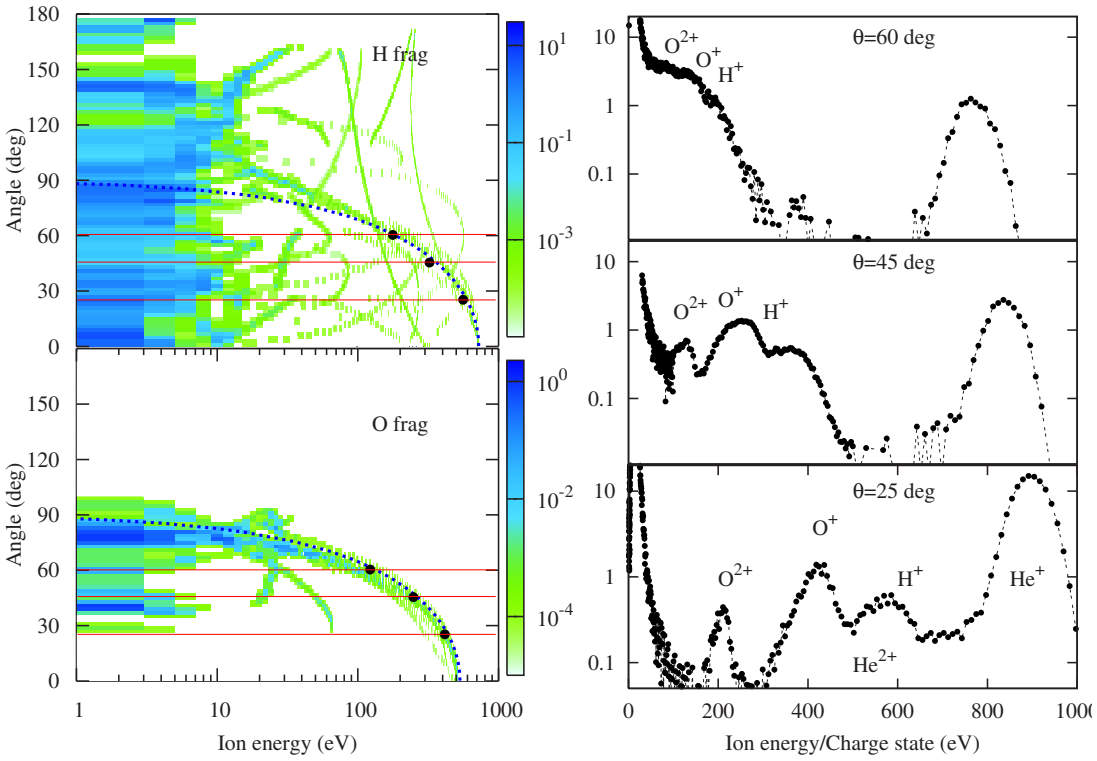

FIG. 8. (Color online) Spectra of fragments ejected in 1 keV $^3He^{2+}+H_2O$ collisions as a function of the ion energy and ejection and/or scattering angle. The END results for proton and oxygen fragments are given in the left-hand panels. The dashed lines are results based on two-body kinematics (see text). The solid circles represent the locations of binary-collision peaks from the experimental spectra [26], which are given at the right-hand side for the observation angles of 25°, 45°, and 60°. The horizontal lines at 25°, 45°, and 60° on the left panels are to guide the eye.

analysis allow us to divide the ions fragmentation energy in two regions.

1. Binary collisions

In the left-hand side of Fig. 8, we present our theoretical results for 1 keV He^{2+} projectiles in a two-dimensional density plot of the fragment emission kinetic energy and ejection angle with respect to the incoming beam. The right-hand graphs of Fig. 8 shows experimental results [26] for emission angles of 25°, 45°, and 60°. The experimental spectra, obtained at relatively high energies, show distinct peaks that can be attributed to binary collisions.

A binary collision involves impact parameters near an atomic center, so that the interaction between the projectile and a single atom of the molecular target dominates. In the two-dimensional plots of Fig. 8 the binary collisions occur in a region with relative large fragment energies of >100 eV. In this binary-collision regime we observe several branches, each one involves a one-to-one correspondence between the emission energy and angle of the fragments.

A closer inspection of the theoretical data shows that these branches originate from different target orientations. Most branches are due to successive binary collisions, where the projectile hits an atom in a violent collision followed by second violent collision of the recoil atom or projectile with another target atom. However, some of the branches are the result of three- or four-body collisions induced by the projectile when hitting a water molecule atom which consequently hits other atom(s) in the molecule, modifying, thus, its kinetic energy and scattering angle. We expect that in a finer orientation grid these branches will be smoothed out.

However, we expect that the most pronounced branch associated with a single binary collision will not be smoothed out and, hence, remain dominant. This branch can be identified by data derived from two-body kinematics based on conservation of energy and momentum, i.e., each angle corresponds to a single energy given by a well-known kinematic formula (e.g, see Refs. [25,26]). In Fig. 8 the results of this two-body formula are shown as a dashed line on top of the END results. The two-body approximation agrees with the END results particularly well at high emission energies of the fragments where binary collisions dominate.

Moreover, this branch compares well to the spectra obtained from Ref. [26]. The position of the experimental peaks are plotted as solid circles together with the theoretical data to show the good agreement between the experiment and theory. In fact, closer inspection of the data shows that the agreement between the experimental data and END theory is better than the corresponding agreement with the two-body formula. This shows that END theory adequately accounts for multibody effects inherent in the experimental data. Also, it becomes evident that the multibody effects depend on the target orientation. Thus, the experimental peaks labeled on the right panel appear to have contributions from both the O and H ions coming from different target orientations.

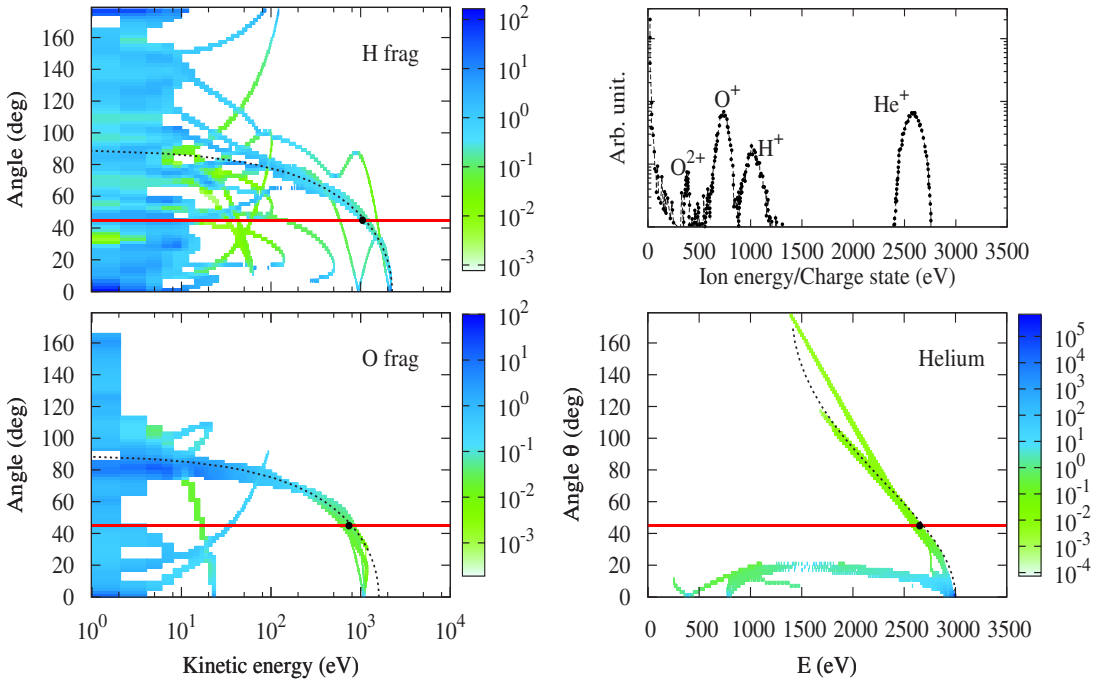

FIG. 9. (Color online) Fragmentation spectra for 3 keV $^3He^+ + H_2O$ collisions as a function of the ion energy and ejection and/or scattering angle. The END results for hydrogen and oxygen fragments (left-hand side) and scattered helium projectiles (right-hand side) are shown in density plots. In the top panel on the right-hand side an experimental spectrum [25] is depicted for an observation angle of 45°. In the density plots the dashed lines are results based on two-body kinematics and the solid circles represent the locations of binary-collision peaks from the experimental spectrum. The horizontal line at 45° is to guide the eye.

In Fig. 9, we show the fragmentation of water by 3 keV $^3He^+$ projectiles, where we distinguish several branches. For instance, in the right-hand panel (labeled "Helium"), which shows the END results for the scattered helium, one finds different branches between 0° and 25° originating from binary collisions with the hydrogen atoms of the water molecule. Moreover, there is a diagonal branch starting at 180° and ending at 0° in the high collision energy region. The origin of this branch is due to single binary collisions with the oxygen atom of water as indicated by the dashed line representing results based on two-body kinematics. Also, we see that the END results compare well with the experimental data [25] given in the top panel on the right-hand side.

The oxygen panel on the left-hand side (labeled "O frag") shows one dominant branch originating from binary collisions with $^3He^+$. This branch has contributions from all target orientations. The other branches at lower energies arise from binary collisions with the hydrogens and only for the I1 and IIb2 orientation. This occurs also for 5.0 keV, while for 1.0 keV only the IIb2 orientation is involved.

The situation is less clear for the hydrogen fragments shown on the left-hand side (labeled "H frag"). There are numerous superimposed branches, which may be smoothed out with a finer grid of target orientations. The closely lying branches at high emission energies are due to single binary collisions in accordance with experimental data and the results based on two-body kinematics (dashed line). Finally we note that a detailed analysis of individual trajectories reveal that the low-energy hydrogen fragment frequently arise from binary collisions of $^3He^+$ with oxygen involving relatively small impact parameters.

2. Soft collisions

Next, we focus on the soft-collision regime characterized by fragments of low energies (<100 eV). In the angular distribution the observed peaks are primarily interpreted within the framework of a Coulomb explosion of the ionized target. That is, the Coulomb repulsion felt by the nuclei forming the H_2O^{2+} molecule after the loss of 2 electrons. Figure 10 compares theoretical fragmentation spectra for the system 5 keV $^3He^{2+} + H_2O$ with the experimental data of Sobocinski [29]. For the experimental spectra the detection angles are 45°, 90°, and 135°, as indicated.

Following previous studies [61], the peaks centered at 6 eV and 15 eV are attributed to H^+ fragments from the dissociation channels $H^+ + OH^+$ and $H^+ + O^+ + H^0$, respectively. However, we note that with the theoretical results we find no evidence for the $H^+ + OH^+$ fragmentation channel for the $^3He^{2+}$ projectile case for the set of impact parameters and target orientations selected in these calculations, probably due to the small probability for such a channel [30,61]. The dissociation channel $H^+ + H^+ + O^0$, which also gives rise to H^+ fragments near 5 eV, has been observed to be weak [61]. The H^+ fragments resulting from the dissociation channels $H^+ + O^+ + H^+$ and $H^+ + O^{2+} + H$, which arise due to the double capture plus ionization, have been observed experimentally at 18 eV [28] and 28 eV [25], respectively. However, due to the lack of the adequate treatment of the ionization channel in the END, we do not see these processes. It should be added that single electron capture accompanied by excitation may lead to dissociation of H_2O^{+*} ions, which results in the emission of H^+ ions with energies near 3.5 eV [28]. This

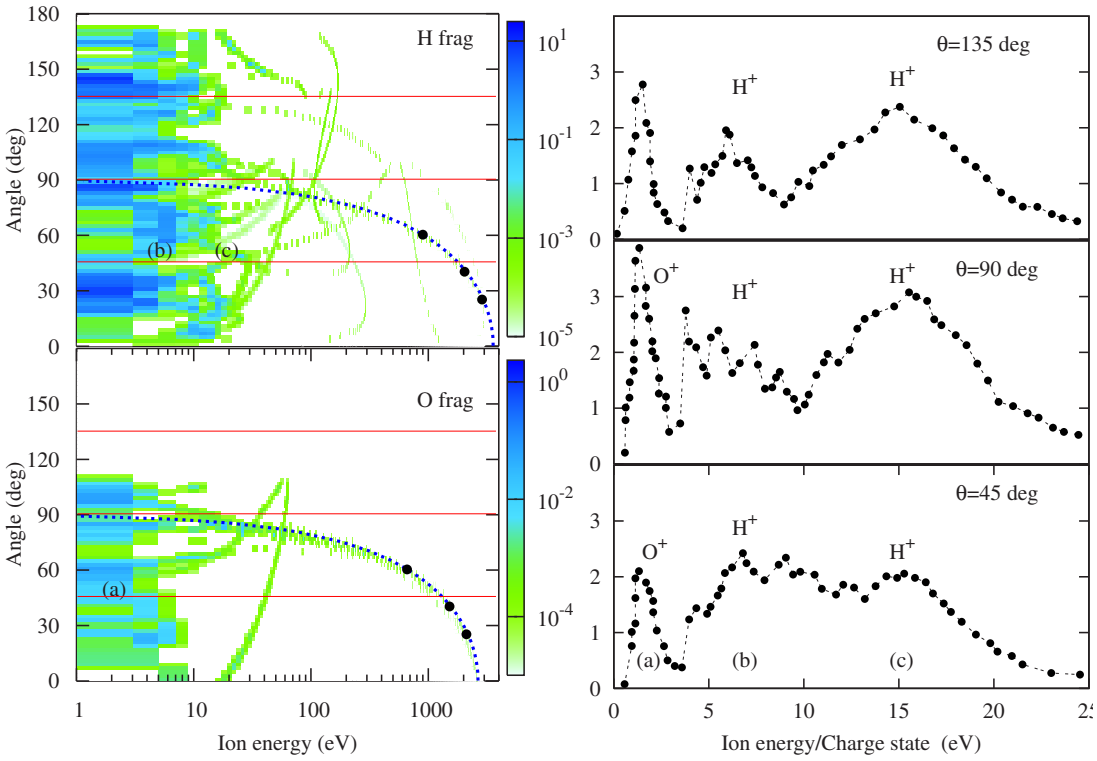

FIG. 10. (Color online) Spectra of fragments ejected in 5 keV $^3He^{2+}+H_2O$ collisions as a function of the ion energy and ejection and/or scattering angle. The END results for proton and oxygen fragments are given in the left-hand panels. The solid circles represent the locations of binary-collision peaks from Ref. [26]. The dashed lines are the result from two-body kinematics. In the right-hand panels experimental spectra [29] are given for observation angles of 45°, 90°, and 135°. The horizontal lines at 45°, 90°, and 135° on the left panels are to guide the eye.

does not appear to be a significant fragmentation channel (see Fig. 10)

Returning to the theoretical data, we note an asymmetry in the emission of the oxygen fragments with respect to the angle of 90°. In the low ion energy region, the oxygen fragments are ejected in the angular range of $25° < \theta < 100°$, wherein two peaks are found at $\theta \sim 40°$ and $\theta \sim 80°$. This 90° asymmetry also occurs, in a less pronounced way, for the H^+ and H fragments which shows three peaks: one at $\theta \sim 40°$, the second at $\theta \sim 75° - 90°$, and the third at $\theta \sim 140°$. The latter is more pronounced than the one at $\theta \sim 40°$. There is also an apparent gap at $\theta \gtrsim 160°$.

The broad experimental H^+ fragment peak around 15 eV is well reproduced for the 135° scattering, while the peak observed at 90° is predicted by theory to occur for slightly greater angles and the broad peak observed at 45° is calculated to occur at slightly smaller angles.

The pronounced peaks at $\theta \sim 40°$ and $\sim 140°$ predicted by END theory for the H^+ and H fragments are barely observed in the experimental results [29]. However, the experiment [29] shows a maximum near 90° in fair agreement with the narrow peak predicted by the theory. We assume that the sharpness of the peaks in the theoretical results is produced by effects due to the coarse target orientation grid. The choice of the minimal set of orientations fortuitously places the OH bond at roughly 45° and 90° with respect to the beam. A more detailed study with a finer orientational grid is required in order to make a more definite conclusion on the mechanism of dissociation (fragmentation) of the OH bond.

Coming back to Fig. 9, we focus our attention on the fragmentation of water by 3 keV He^+ impact in soft collisions. Most of the oxygen fragments are ejected at angles around 75°–85° in the low-energy region, while the hydrogen fragments are emitted mostly around 45°, 90°, and 135°. For the present case of $^3He^+$ ions, we see formation of OH fragments. The majority of the OH fragments have energies below 5.0 eV and are ejected at angles around 50°–135°. In particular, we find the production of the hydroxyl group to increase with decreasing collision energy. The rest of the low-energy hydrogen fragments arise from larger impact parameter collisions leading to electron transfer followed by dissociation of the water molecule.

F. Model for low-energy peaks

The fragmentation spectra peaks can be understood in the low ion energy range as due to Frank-Condon excitation into the H_2O^{2+} water-molecule states that then decay into fragments. For the water-molecule ion, H_2O^{2+}, we must distinguish between two geometries. One when the excitation is fast enough that the molecule keeps its C_{2v} geometry, and one when the time scale is low enough that it relaxes to its linear configuration, $D_{\infty h}$ before fragmentation. From conservation of energy, we have, for the fragmentation channel $2H^+ + O$, that

TABLE II. Kinetic energy of the fragments (eV) for the two configuration C_{2v} and $D_{\infty h}$ and for three different dissociation channels (see text for discussion). The electronic energies obtained at the Hartree-Fock level, as required by Eqs. (5)–(9) are $E(O)=-74.8027$, $E(O^+)=-74.3648$, and $E(OH^+)=-74.8499$, all in a.u. (1 a.u.=27.2 eV). The excited states energies for $E(H_2O^{2+})$ are taken from Ref. [61].

	$2H^+ + O$				$H^+ + H + O^+$				$OH^+ + H^+$	
Hartree-Fock energies (a.u.)	C_{2v}			$D_{\infty h}$	C_{2v}			$D_{\infty h}$		
H_2O^{2+}	ΔE	$K(0)$	$K(H^+)$	$K(H^+)$	ΔE	$K(0^+)$	$K(H^+)$	$K(H^+)$	ΔE	H^+
$E(^1A_1)=-74.6120$	5.2	0.2	2.5	2.6	6.9	0.3	3.3	3.5	6.3	6.3
$E(^3B_1)=-74.6873$	3.1	0.1	1.5	1.6	4.8	0.2	2.3	2.4	4.4	4.4
$E(^1B_1)=-74.5826$	6.0	0.3	2.9	3.0	7.7	0.4	3.7	3.9	7.3	7.3

$$\Delta E = E(H_2O^{2+}) - E(O) = K(O) + 2K(H^+), \tag{5}$$

where K is the kinetic energy of the fragment. For the C_{2v} symmetry, we assume that the H^+ departs in the bond direction, and from conservation of momentum, we find that

$$K(O) = \frac{\Delta E}{\left(1 + \frac{1}{\gamma}\frac{M_O}{M_H}\right)} \tag{6}$$

and

$$K(H^+) = \frac{\Delta E}{\left(2 + 2\gamma\frac{M_H}{M_O}\right)}. \tag{7}$$

Here, the factor $\gamma=2\cos^2(\theta/2)\approx(3/4)$, where $\theta=104.5°$ is the bond angle for water in the C_{2v} configuration and M_i is the mass of the ith fragment. For the configuration $D_{\infty h}$, we assume that the oxygen atom remains at rest and the H^+ break in opposite direction. Thus

$$K(H^+) = \frac{\Delta E}{2}. \tag{8}$$

For the case of the dissociation channel $H+H^+ + O^+$, the situation is similar as to the previous case with ΔE set to $\Delta E = E(H_2O^{2+}) - E(O^+) - E(H)$ in the previous equations for both geometry dissociation.

Finally, we treat the case for $OH^+ + H^+$ for which $\Delta E = E(H_2O^{2+}) - E(OH^+)$ and since the dissociation is linear, we obtain

$$K(H^+) = \frac{\Delta E}{\left(1 + \frac{M_H}{M_{OH}}\right)}. \tag{9}$$

The electronic energies for the different excited states of the molecular ion H_2O^{2+} were obtained at the Hartree-Fock level (SCF) by Richardson *et al.* [61] for three different excited states ($^1A_1$, $^3B_1$, and $^1B_1$). Within our approach we calculate the energies for O, O^+, and OH^+ at the same level of theory. In Table II, we show E for the water molecular ion and the respective dissociation fragments as required in the previous equations. Also, we give the resulting kinetic energies for the peaks of the fragments. We see that the results of Fig. 10, for the low ion energies, arise from dissociation of both C_{2v} and $D_{\infty h}$ geometries from the lowest excited states of H_2O^{2+}. For the case of H^+, in the 1–4 eV ion energy range, they arise from the $O+2H^+$ and $O^+ + H^+ + H$ channels in the C_{2v} and $D_{\infty h}$ geometries, as mentioned previously. Meanwhile the $OH^+ + H^+$ channel explains the peaks in the ion energy spectra in the 4–7 eV, in agreement with Richardson *et al.* [61]. The 12 and 15 eV peaks seems to arise from higher excitations of the H_2O^{2+} ion molecule. Another point to note is that according to Richardson *et al.* [61], the energies calculated within the Hartree-Fock model are 3 to 5 eV higher than the experimental values due to electronic correlation. This would shift the kinetic energy peaks to lower energies. One should note that this analysis is based on a simple "static" excitation analysis using potential energy surfaces within a Hartree-Fock level of theory, and does not include the momentum transfer to the nuclei due to the coupling with other atoms or with the electrons, which are included in END.

IV. CONCLUSIONS

Using the END approach, we investigate charge transfer and fragmentation in collisions of $^3He^+$ and $^3He^{2+}$ with H_2O as a function of the projectile energy. The END calculations are based on a quantum mechanical treatment to solve the time-dependent Schrödinger equation, which involves the dynamics of both the electrons and nuclei. The calculations are performed for a discrete set of molecular orientations which, in turn, are used to evaluate orientation averaged results. To obtain information about the projectile charge state, the electronic wave function was projected on specific final states.

For $^3He^{2+}$ impact, probabilities for single and double electron capture are found to be consistent with results based on a binomial distribution. Differential cross sections for scattering of $^3He^+$ and $^3He^{2+}$ projectiles are calculated in good agreement with experimental data. Furthermore, total cross sections for single and double electron capture are evaluated. From the agreement of the theoretical and experimental capture cross sections, we conclude that the limited number of molecular orientations is adequate for the evaluation of the present capture cross sections. This gives confidence that END is a suitable method to predict reliable cross sections for complex ion-molecule collisions, which are relevant to astrophysical and biological systems.

Particular attention is devoted to mechanisms leading to fragmentation of the water molecules. For emitted oxygen and hydrogen fragments the relation between the emission angle and energy is presented in two-dimensional density plots. In the binary collisions regime, where fragments of relative high energies ($\gtrsim$100 eV) are produced, several discrete branches are observed that involve a one-to-one correspondence between emission angle and energy. The major branch is found to be in good agreement with results derived from two-body kinematics characteristic for binary collisions.

In the soft-collision regime, where fragments of lower energies are produced, the oxygen and proton fragments are continuously distributed in the two-dimensional density plots. For $^3He^{2+}$ impact, the angular distribution of the emitted protons exhibit peaks at distinct angles including 90°. Indeed, the angular distribution of the measured protons shows a maximum near 90° which, however, is significantly broader than the theoretical peak. This finding suggests that the theoretical reproduction of detailed experimental features require a finer grid of molecular orientations. Therefore, further studies are needed to investigate the influence of the finite grid size.

ACKNOWLEDGMENTS

We would like to thank Thomas Schlathölter and Belá Sulik for helpful discussions. We acknowledge support within the Cost P9 Action of the European Science Foundation. E.D. and Y.O. acknowledge the support of NSF Grant No. 0513386. O.Q. acknowledges the Belgian National Fund for Scientific Research.

[1] C. M. Lisse *et al.*, Science **274**, 205 (1996).
[2] T. E. Cravens, Geophys. Res. Lett. **24**, 105 (1997).
[3] V. Kharchenko and A. Dalgarno, J. Geophys. Res. **105**, 18 (2000).
[4] J. B. Wargelin and J. J. Drake, Astrophys. J. Lett. **546**, L57 (2001).
[5] J. E. Biaglow, in *Radiation Chemistry: Principles and Applications*, edited by M. A. Farhataziz and J. Rodgers (VCH, New York, 1987), p. 527.
[6] G. Bishof and F. Linder, Z. Phys. D: At., Mol. Clusters **1**, 303 (1986).
[7] F. B. Yousif, B. G. Lindsay, and C. J. Latimer, J. Phys. B **21**, 4157 (1988).
[8] S. Cheng, C. L. Cocke, V. Frohne, E. Y. Kamber, J. H. McGuire, and Y. Wang, Phys. Rev. A **47**, 3923 (1993).
[9] A. Remscheid, B. A. Huber, and K. Wiesmann, Nucl. Instrum. Methods Phys. Res. B **98**, 257 (1995).
[10] F. Frémont, C. Bedouet, M. Tarisien, L. Adoui, A. Cassimi, A. Dubois, J.-Y. Chesnel, and X. Husson, J. Phys. B **33**, L249 (2000).
[11] P. Sobocinski, J. Rangama, J.-Y. Chesnel, M. Tarisien, L. Adoui, A. Cassimi, X. Husson, and F. Frémont, in *Conference on Accelerators and their Application in Research and Industry*, edited by J. Duggan, AIP Conference Proceedings No. 576 (AIP, New York, 2001), pp. 114–117.
[12] P. Sobocinski, J. Rangama, G. Laurent, L. Adoui, A. Cassimi, J.-Y. Chesnel, A. Dubois, D. Hennecart, X. Husson, and F. Frémont, J. Phys. B **35**, 1353 (2002).
[13] I. Ben-Itzhak, E. Wells, K. D. Carnes, V. Krishnamurthi, O. L. Weaver, and B. D. Esry, Phys. Rev. Lett. **85**, 58 (2000).
[14] M. Tarisen, L. Adoui, F. Frémont, D. Lelièvre, L. Guillaume, J.-Y. Chesnel, H. Zhang, A. Dubois, D. Mathur, K. Sanjay *et al.*, J. Phys. B **33**, L11 (2000).
[15] H. O. Folkerts, R. Hoekstra, and R. Morgenstern, Phys. Rev. Lett. **77**, 3339 (1996).
[16] I. Ben-Itzhak, K. D. Carnes, D. T. Johnson, P. J. Norris, and O. L. Weaver, Phys. Rev. A **49**, 881 (1994).
[17] C. R. Feeler, C. J. Wood, and R. E. Olson, Phys. Scr. **59**, 106 (1999).
[18] C. R. Feeler, R. E. Olson, R. D. DuBois, T. Schlathöter, O. Hadjar, R. Hoekstra, and R. Morgenstern, Phys. Rev. A **60**, 2112 (1999).
[19] U. Werner, K. Beckord, J. Becker, H. O. Folkerts, and H. O. Lutz, Nucl. Instrum. Methods Phys. Res. B **98**, 385 (1995).
[20] F. Gobet, B. Farizon, M. Farizon, M. J. Gaillard, M. Carré, M. Lezius, P. Scheier, and T. D. Märk, Phys. Rev. Lett. **86**, 3751 (2004).
[21] F. Gobet, S. Eden, B. Coupier, J. Tabet, B. Farizon, M. Farizon, M. J. Gaillard, M. Carré, S. Ouaskit, T. D. Märk *et al.*, Phys. Rev. A **70**, 062716 (2004).
[22] H. Luna and E. C. Montenegro, Phys. Rev. Lett. **94**, 043201 (2005).
[23] U. Werner, K. Beckord, J. Becker, and H. O. Lutz, Phys. Rev. Lett. **74**, 1962 (1995).
[24] O. Abu-Haija, E. Y. Kamber, and S. M. Ferguson, Nucl. Instrum. Methods Phys. Res. B **205**, 634 (2003).
[25] Z. D. Pešić, J.-Y. Chesnel, R. Hellhammer, B. Sulik, and N. Stolterfoht, J. Phys. B **37**, 1405 (2004).
[26] P. Sobocinski, Z. D. Pešić, R. Hellhammer, N. Stolterfoht, B. Sulik, S. Legendre, and J.-Y. Chesnel, J. Phys. B **38**, 2495 (2005).
[27] B. Seredyuk, R. W. McCullough, H. Tawara, H. B. Gilbody, D. Bodewits, R. Hoekstra, P. Sobocinski, Z. D. Pešić, R. Hellhammer, B. Sulik *et al.*, Phys. Rev. A **71**, 022705 (2005).
[28] F. Alverado, R. Hoekstra, and T. Schlathölter, J. Phys. B **38**, 4085 (2005).
[29] P. Sobocinski, Z. D. Pešić, R. Hellhammer, D. Klein, B. Sulik, J.-Y. Chesnel, and N. Stolterfoht, J. Phys. B **39**, 927 (2006).
[30] A. M. Sayler, M. Leonard, K. D. Carnes, R. Cabrera-Trujillo, B. D. Esry, and I. Ben-Itzhak, J. Phys. B **39**, 1701 (2006).
[31] C. J. Wood and R. E. Olson, Phys. Rev. A **59**, 1317 (2001).
[32] R. Car and M. Parrinello, Phys. Rev. Lett. **55**, 2471 (1985).
[33] B. Brena, D. Nordlund, M. Odelius, H. Ogasawara, A. Nilsson, and L. G. M. Pettersson, Phys. Rev. Lett. **93**, 148302 (2004).
[34] I. Anusiewicz, J. Berdys, M. Sobczyk, P. Skurski, and J. Simons, J. Phys. Chem. A **108**, 11381 (2004).
[35] J. Berdys, P. Skurski, and J. Simons, J. Phys. Chem. B **108**, 5800 (2004).

[36] E. Runge and E. K. U. Gross, Phys. Rev. Lett. **52**, 997 (1984).
[37] J. M. Tao and J. P. Perdew, Phys. Rev. Lett. **95**, 196403 (2005).
[38] M. V. Faassen, Int. J. Mod. Phys. B **20**, 3419 (2006).
[39] J. B. Delos, Rev. Mod. Phys. **58**, 287 (1981).
[40] E. Deumens, A. Diz, H. Taylor, and Y. Öhrn, J. Chem. Phys. **96**, 6820 (1992).
[41] E. Deumens and Y. Öhrn, J. Phys. Chem. **92**, 3181 (1988).
[42] *Time-Dependent Quantum Molecular Dynamics*, edited by J. Broeckhove and L. Lathouwers (Plenum, New York, 1992).
[43] E. Deumens and Y. Öhrn, J. Chem. Soc., Faraday Trans. **93**, 919 (1997).
[44] E. Deumens and Y. Öhrn, J. Phys. Chem. A **105**, 2660 (2001).
[45] E. Deumens, A. Diz, R. Longo, and Y. Öhrn, Rev. Mod. Phys. **66**, 917 (1994).
[46] D. J. Thouless, Nucl. Phys. **21**, 225 (1960).
[47] E. Deumens, T. Helgaker, A. Diz, H. Taylor, J. Oreiro, B. Mogensen, J. A. Morales, M. C. Neto, R. Cabrera-Trujillo, and D. Jacquemin, *ENDYNE version 5 Software for Electron Nuclear Dynamics*, Quantum Theory Project, University of Florida, Gainesville, FL 32611-8435, http://www.qtp.ufl.edu/endyne.html (2002).
[48] D. Jacquemin, J. A. Morales, E. Deumens, and Y. Öhrn, J. Chem. Phys. **107**, 6146 (1997).
[49] T. H. Dunning, J. Chem. Phys. **90**, 1007 (1989).
[50] D. E. Woon and T. H. Dunning, J. Chem. Phys. **100**, 2975 (1994).
[51] R. S. Mulliken, J. Chem. Phys. **23**, 1833 (1955).
[52] R. Cabrera-Trujillo, Y. Öhrn, E. Deumens, and J. R. Sabin, Phys. Rev. A **62**, 052714 (2000).
[53] I. Ben-Itzhak, T. J. Gray, J. C. Legg, and J. H. McGuire, Phys. Rev. A **37**, 3685 (1988).
[54] J. B. Greenwood, R. S. Mawhorter, I. Čadež, J. Lozano, S. J. Smith, and A. Chutjian, Phys. Scr., T **T110**, 358 (2004).
[55] M. E. Rudd, A. Itoh, and T. V. Goffe, Phys. Rev. A **32**, 2499 (1985).
[56] J. B. Greenwood, A. Chutjian, and S. J. Smith, Astrophys. J. **529**, 605 (2000).
[57] L. I. Schiff, Phys. Rev. **103**, 443 (1956).
[58] R. Cabrera-Trujillo, J. R. Sabin, Y. Öhrn, and E. Deumens, Phys. Rev. A **61**, 032719 (2000).
[59] R. G. Newton, *Scattering Theory of Waves and Particles* (Springer-Verlag, New York, 1982).
[60] B. H. Bransden and M. R. C. McDowell, *Charge Exchange and the Theory of Ion-Atom Collisions* (Clerendon Press, Oxford, 1992).
[61] P. J. Richardson, J. H. D. Eland, P. G. Fournier, and D. L. Cooper, J. Chem. Phys. **84**, 3189 (1986).